



## Supplementary Materials for

### **Structure of a prehandover mammalian ribosomal SRP•SRP receptor targeting complex**

Kan Kobayashi,\* Ahmad Jomaa,\* Jae Ho Lee, Sowmya Chandrasekar,  
Daniel Boehringer, Shu-ou Shan, Nenad Ban<sup>†</sup>

\*These authors contributed equally to this work.

<sup>†</sup>Corresponding author. Email: ban@mol.biol.ethz.ch

Published 22 March 2018 on *Science* First Release

DOI: 10.1126/science.aar7924

#### **This PDF file includes:**

Materials and Methods  
Figs. S1 to S14  
Table S1  
References

## Materials and Methods

### Sample preparation

Mammalian RNC harboring the signal sequence was prepared basically as described (12, 27). The DNA fragment having sequences for T7 promoter, Kozak, and 3 × FLAG tag, followed by LDKLIRVGIILVLLIWGTVLLLKSIPHHSNTPDYQEPNSNYTNDGKLKVSFSVVRNNTFHPKYHELH (hydrophobic signal sequence is underlined.) was cloned into EcoRI/PstI site of pUC57 plasmid (GenScript). After the digestion of the plasmid by PstI, mRNA was generated by in vitro transcription using T7 polymerase. The synthesized mRNA was purified by LiCl precipitation followed by ethanol precipitation. The purified mRNA was translated in the Flexi® Rabbit Reticulocyte Lysate System (Promega) at the mRNA concentration of 214 ng/μL for 25 min at 32°C. Then, 0.5 mL of ANTI-FLAG® M2 Affinity Gel (SIGMA-ALDRICH) equilibrated with buffer A (50 mM HEPES-KOH, pH 7.6, 100 mM KCl, 5 mM MgCl<sub>2</sub>) was added to 4.7 mL of the translation reaction product and gently mixed for 2 h at 4°C. Following the removal of the lysate, the gel was washed by 10 mL of buffer B (50 mM HEPES-KOH, pH 7.6, 500 mM KCl, 5 mM MgCl<sub>2</sub>) and then by 10 mL of buffer A. Then, RNCs were eluted by adding 5 mL of buffer A containing 0.1 mg/mL 3 × FLAG® Peptide (SIGMA-ALDRICH). The elution was collected with 0.5 mL/fraction. Fractions containing RNC were ultracentrifuged using a TLA55 rotor (Beckman Coulter) at 50,000 rpm at 4°C for 2 h, and the RNC pellet was resuspended into buffer C (50 mM HEPES-KOH, pH 7.6, 100 mM KOAc, 5 mM Mg(OAc)<sub>2</sub>). The final concentration of RNC was 1 μM and stored at -80 °C.

Mammalian SR was prepared basically as described (26). The gene coding full-length rabbit SRα and the cytosolic GTPase domain of rabbit SRβ (residues from 60 to 271) was cloned into pET20b and pET24a (Novagen), respectively. SRα and SRβ were co-expressed in *Escherichia coli* BL21-SI strain (Invitrogen) having pRARE plasmid (Novagen). Produced SRα protein has an N-terminal His-tag for purification. Cells were cultured at 37°C in a 2.5 L medium containing 1.6% tryptone and 1% yeast extract. At OD<sub>600</sub> = 0.5, NaCl and IPTG was added to the final concentration of 300 mM and 0.5 mM, respectively. After culturing cells for 2 h at 37°C, they were collected by centrifugation at 5,000 g for 12 min. Cells were suspended into 50 mL of buffer D (20 mM Tris-HCl, pH 7.6, 500 mM NaCl, 20 mM Imidazole, 5 mM MgCl<sub>2</sub>, 1 mM 2-mercaptoethanol, 0.1 mM phenylmethylsulfonyl fluoride) and lysed by sonication. After pelleting cell debris by centrifugation at 48,000 g for 40 min, the supernatant fraction was applied onto 5 mL HisTrap HP column (GE Healthcare) equilibrated with buffer E (20 mM Tris-HCl, pH 7.6, 500 mM NaCl, 20 mM Imidazole, 5 mM MgCl<sub>2</sub>, 1 mM 2-mercaptoethanol). After washing the column by 75 mL of buffer E, SR was eluted by 30 mL of buffer F (20 mM Tris-HCl, pH 7.6, 500 mM NaCl, 300 mM Imidazole, 5 mM MgCl<sub>2</sub>, 1 mM 2-mercaptoethanol). Elution was collected with 5 mL/fraction. Two fractions containing SR were mixed, and then 23 mL of buffer G (20 mM Tris-HCl, pH7.0, 1 mM DTT) was added. The sample was applied to 5 mL HiTrap SP HP column (GE Healthcare) equilibrated with buffer H (20 mM Tris-HCl, pH7.0, 150 mM NaCl, 1 mM DTT). After washing the column by 15 mL of buffer H, SR was eluted by a 50 mL of NaCl linear gradient from 150 mM to 1 M. Fractions containing SR were mixed and concentrated with Amicon® Ultra-15 (Merck Millipore Ltd) to 5 mL. The concentrated

sample was applied to HiLoad 16/60 Superdex200 (GE Healthcare) equilibrated with buffer C. Fractions containing SR were mixed and concentrated with Amicon® Ultra-15 (Merck Millipore Ltd). After pelleting aggregated proteins by centrifugation, the concentration of the supernatant fraction was 37.5  $\mu$ M and stored at -80 °C.

Sec61p was purified from the pig pancreas microsomes essentially as previously described (39).

#### Cryo-EM data collection

RNC was mixed with purified dog SRP (tRNA probes), and incubated for 15 min at 25°C in the presence of 0.25% digitonin and 2 mM GMPPNP. SR was mixed with Sec61p, and incubated for 15 min at 25°C. Then, they were mixed and further incubated for 15 min at 25°C. We observed that the targeting complex assembled more efficiently in the presence of Sec61p, allowing us to collect a dataset with larger number of particles contributing to the final cryo-EM map. After that, the sample was incubated on ice. The final sample contained 200 nM RNC, 245 nM SRP, 1  $\mu$ M SR, and 1  $\mu$ M Sec61p. Cryo-EM grids were prepared with the Vitrobot equilibrated at 4 °C and 100% relative humidity. 5  $\mu$ L of the sample was applied onto the Quantifoil R2/2 holey carbon grid, which had been coated with thin carbon film and glow-discharged. The sample was incubated on the grid for 2 min. After blotting for 10 sec, grids were flash-frozen in liquid ethane.

Data collection was performed on a Titan Krios electron microscope (FEI Company) at 300 kV, using the EPU software (FEI Company) for automated data acquisition. Data were collected at a defocus of -1.2 to -3  $\mu$ m at a magnification of 100,719x. Micrographs were recorded on Falcon II direct electron detector (FEI Company) as movie stacks. The exposure time for each movie stack was 1.4 sec, corresponding to an electron dose of  $\sim$ 40 electrons/ $\text{\AA}^2$  fractionated into 25 frames (55 msec/frame). After discarding the first and last frames, drift and gain corrections and dose-weighting were performed with MotionCor2 (40).

#### Data processing and map calculation

Contrast transfer function (CTF) was calculated from motion-corrected and non-dose-weighted images using CTFFIND4 (41). After removing images having poor CTF quality, ribosome particles were semi-automatically picked from motion-corrected and dose-weighted images using Batchboxer implemented in EMAN (42). The following processing scheme of particle images by classification, refinement, and post-processing were performed using RELION2.0 (43, 44) (Fig. S1). Two datasets were collected and processed using an identical image-processing scheme. 493,114 particle images from dataset 1 and 282,676 from dataset 2 were extracted and binned four-fold (5.56  $\text{\AA}$ /pixel) and were processed by the two-dimensional (2D) classification and only 2D class averages of 80S ribosomes depicting high-resolution features were selected. From dataset 1, 378,316 particle images were processed by the three-dimensional (3D) auto-refinement option against the map of the rabbit ribosome (EMD-2620) (45) low-pass filtered to 60  $\text{\AA}$  as the reference. The aligned particle images were processed by an initial 3D classification without image alignment focused on the SRP S domain. 50,823 particle images were selected yielding a class having strong signals of SRP RNA and the NG heterodimer at the SRP RNA distal site, and two-fold binned images (2.78  $\text{\AA}$ /pixel) were

processed by the 3D auto-refine with a mask on the 60S subunit, SRP and SR. To further improve the densities of SRP·SR, a 2<sup>nd</sup> 3D classification step focusing on the SRP RNA distal site only was performed, followed by a 3<sup>rd</sup> 3D classification step with the signal outside of the distal site subtracted from the images (46). 26,601 particle images were selected depicting the best class with the strongest density of SRP and SR and were combined with 19,207 particle images selected from the dataset 2 after following identical classification scheme as in dataset 1. Full-size particle images (1.39 Å/pixel) were processed by the 3D auto-refine, and generated the map of 3.8 Å resolution on average at a gold-standard FSC = 0.143 after post-processing. The overall average resolution of the final map is 3.7 Å from 45,800 particles after per-particle CTF correction using GCTF (47), 3D auto-refine and post-processing (Fig. S2A). The local resolution of the map was calculated using BLOCREX (48, 49) implemented in RELION2.0 (43) (Fig. S2C). To better visualize the density of SRP68/72 PBD attached to the SRP RNA, an additional classification was done by focusing on this region using particles after the 2<sup>nd</sup> classification (Fig. S5A). 26,515 and 21,295 particles were selected from dataset 1 and 2, respectively, depicting the strongest density of the SRP68/72 PBD. Full-size images of these particles were processed by the 3D auto-refine and the resulting overall average resolution of the map was 3.9 Å after post-processing. All maps were sharpened using auto-bfac option in RELION.

### Structure model building

For the model building of SRP·SR·RNC complex, previously reported structure models were docked as a rigid body into the map using UCSF Chimera (50) and, if necessary, manually corrected using COOT (51). The models of RNC, hydrophobic signal sequence-bound SRP54 M domain, SRP Alu domain and P-site tRNA were built into the cryo-EM map based on the model of porcine RNC bound to SRP (PDB ID: 3JAJ) (27) and the crystal structure of the SRP54 M domain bound to SRP RNA (PDB ID: 1MFQ) (52) and were manually adjusted. For the NG heterodimer of SRP54 and SR $\alpha$ , the human NG heterodimer model (PDB ID: 5L3Q) (18) were docked and corrected. For SRX·SR $\beta$ , the heterodimer model (PDB ID: 2FH5) of human SRX and mouse SR $\beta$  bound to GTP (30) was docked, and the helix  $\alpha$ 1x of SRX was modeled based on a homologous structure from yeast (PDB ID: 1NRJ) (34). For the SRP RNA in the S domain, human models were docked (PDB ID: 4P3E for 114-237, and PDB ID: 5M73 for 106-113 and 238-249) and corrected (22, 31). In the SRP RNA docking process, models of SRP19, SRP68 RBD, and SRP72 RBD bound to it in the crystal structures were also fitted as a rigid body. For the hinge region of SRP RNA between S and Alu domains, the SRP RNA model of residues 87-105 and 250-262 (PDB ID: 4UE5) (53) was fitted and corrected. For the SRP68/72 PBD complex, the crystal structure of it (PDB ID: 5M72) (22) was tentatively docked into the map, considering the positions of the highly conserved basic residues (Arg90 and Arg121) of SRP72 PBD, through which it could attach to the SRP RNA (Fig. S5B and S5C). The sequences of SRP and SR component models were changed to those from dog and rabbit, respectively. For the model refinement, the cryo-EM map was converted to the map consisting of the sum of structure factors with blurred phase probabilities in a resolution dependent manner by the figure of merit (FOM) weighting as previously described (54). To remove clashes and regularize the geometry, the model of 60S·SRP·SR was subjected to one cycle of rigid body

refinement with PHENIX (55) (one rigid group for the 60S subunit, NG domains of SRP54 and SR $\alpha$ , SRX, SR $\beta$ , and SRP RNA bound to SRP19, SRP68/72 and SRP54 M domain) and then followed by 11 cycles of individual B-factor and coordinate refinement against FOM weighted experimental electron microscopy phases and back-calculated structure factors using the phased maximum-likelihood (MLHL) target. To maintain good geometry, base pair, Ramachandran, and secondary structure restraints were imposed as previously described (54) due to limited resolution in certain areas. Model refinement and validation statistics of the 60S·SRP·SR and only of the SRP·SR regions are provided in Supplementary Table S1.

#### Biochemical experiments using recombinant SRP and SR

Human SRP54, SRP19, SRP9/14, SR $\alpha\beta\Delta$ TM (lacking nonessential luminal and transmembrane regions of SR $\beta$ ) and SR $\alpha\Delta$ X (lacking SRX·SR $\beta$ ) were expressed in BL21(DE3) strains and purified as described (56-58). Human SRP68/72 was co-expressed in yeast and purified as described in (59). Human SRP RNA (7SL) was *in vitro* transcribed and purified. Wild type and mutant SRP were assembled with modification of the procedures described by (59) and purified over a DEAE-sepharose column.

Elongation arrest activity was measured by titrating wild type or mutant SRP into *in vitro* translation reactions of preprolactin (pPL) in wheat germ extract. Prolactin (PL), which does not contain a signal sequence, was translated in the same reaction to provide an internal standard. Translation was followed for 5 minutes, and the amount of <sup>35</sup>S-methionine labeled pPL relative to PL was analyzed by SDS-PAGE and autoradiography.

Co-translational targeting and translocation of <sup>35</sup>S-methionine labeled pPL into salt-washed, trypsinized rough ER microsome (TKRM) was measured as described (60, 61). The efficiency of translocation for pPL was quantified as:

$$\% \text{Translocation} = \frac{\binom{8}{7} \text{prolactin}}{\binom{8}{7} \text{prolactin} + \text{preprolactin}} \times 100$$

The (8/7) term corrects for the different number of methionines in pPL versus signal sequence-cleaved.

The reciprocally stimulated GTPase activities of SRP and SR variants were measured using a fixed, limiting amount of SRP, varying concentrations of SR, and 100  $\mu$ M GTP doped with  $\gamma$ -<sup>32</sup>P-GTP. Reactions were monitored by thin layer chromatography as described (62). The SR concentration dependencies of observed GTPase rates were fit to the Michaelis-Menten equation to obtain values of  $k_{\text{cat}}$ .

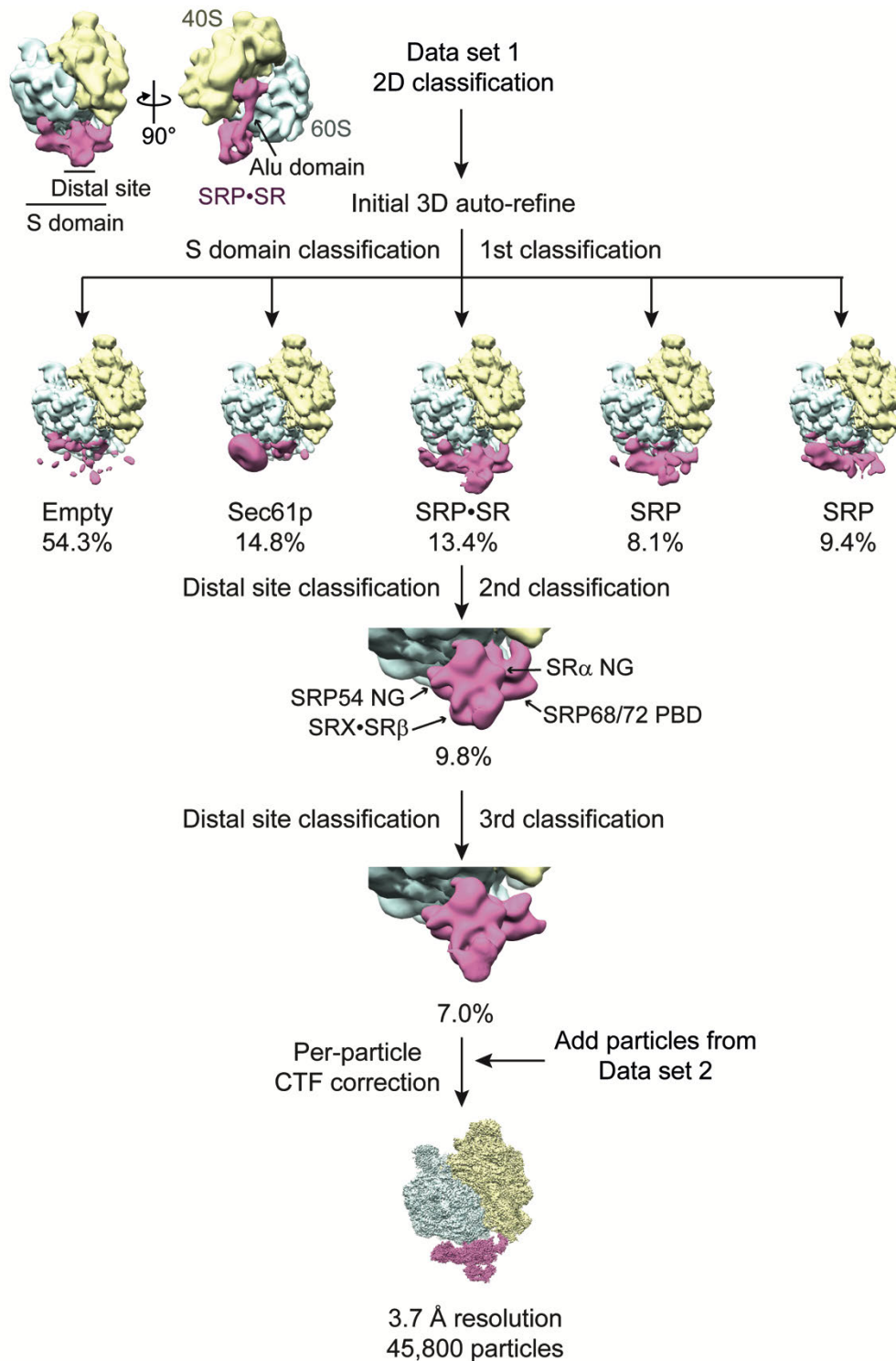


**Fig. S1. 3D image classification scheme.**

3D classification procedure of ribosomal particles from data set 1. SRP·SR, ribosomal 40S and 60S subunits are colored magenta, yellow, and light blue, respectively.

Ribosomal particles from data set 2, classified in the same procedure, were combined with data set 1 before the final refinement step. See Materials and Methods for details.

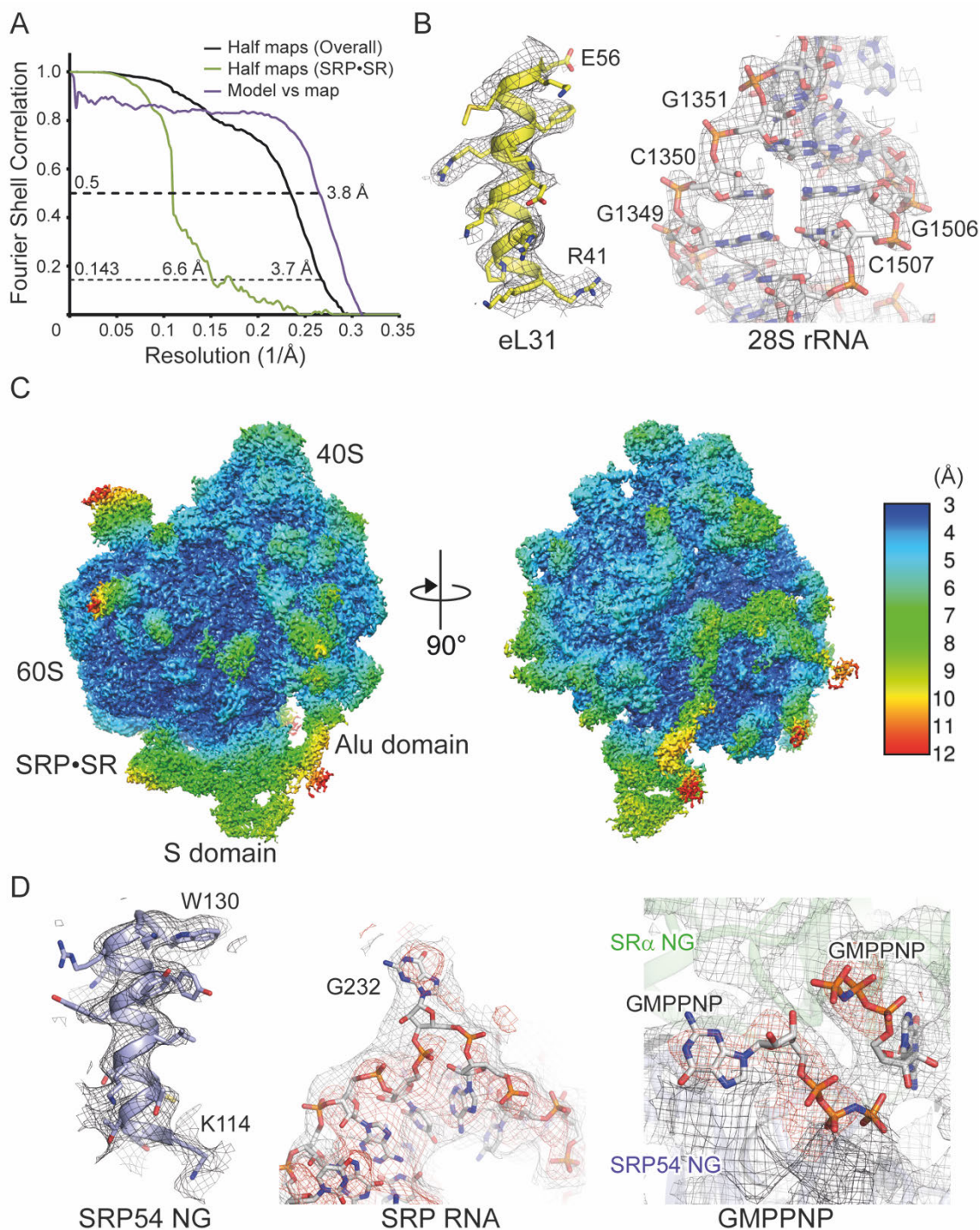


**Fig. S2. Fourier shell correlation curves, representative maps, and local resolution.**

(A) Curves of the Fourier shell correlation (FSC) values between two independently refined half maps for SRP·SR·RNC (black) and for SRP·SR calculated by masking out ribosomal density (green), and that between the map from full data and model (purple). The resolution of SRP·SR·RNC complex and SRP·SR is 3.7 Å and 6.6 Å, respectively based on the resolution criterion cutoff of the gold standard FSC value of 0.143 as implemented in RELION (44). The model correlates with the map to 3.8 Å resolution,

based on the resolution criterion cutoff of the FSC value between the map from full data and model of 0.5 (63). **(B)** Representative maps of the ribosomal protein eL31 helix (Arg41-Glu56) (left) and 28S rRNA region (right) shown in the gray mesh. For eL31, the helix is shown in the cartoon colored yellow, and side chains are in the stick model. 28S rRNA is shown in the stick model. The residue numbering is based on the previous model (PDB ID: 3JAJ) (27) **(C)** The map of SRP·SR·RNC complex low-pass filtered to 3.7 Å resolution is shown from two perpendicular directions. The map is colored to represent the local resolution based on the color bar on the right side. The local resolution of the map was calculated using BLOCRES (48, 49) implemented in RELION2.0 (43). **(D)** Representative maps of the SRP·SR·RNC complex low-pass filtered to 4.5 Å resolution for SRP54 NG domain helix (Lys114-Trp130) (left), SRP RNA (around the flipped-out base G232) (center), and the two GMPPNP molecules bound to NG heterodimer (right). The map of SRP54 is shown in gray mesh, and those of SRP RNA and GMPPNP are shown in two contour levels (gray and red mesh). The helix of SRP54 NG domain is shown in the cartoon colored light blue, and side chains are in the stick model. SRP RNA is shown in the stick model. Two GMPPNP molecules are shown in the stick model, and the NG heterodimer is shown and colored as in Fig. 1C.

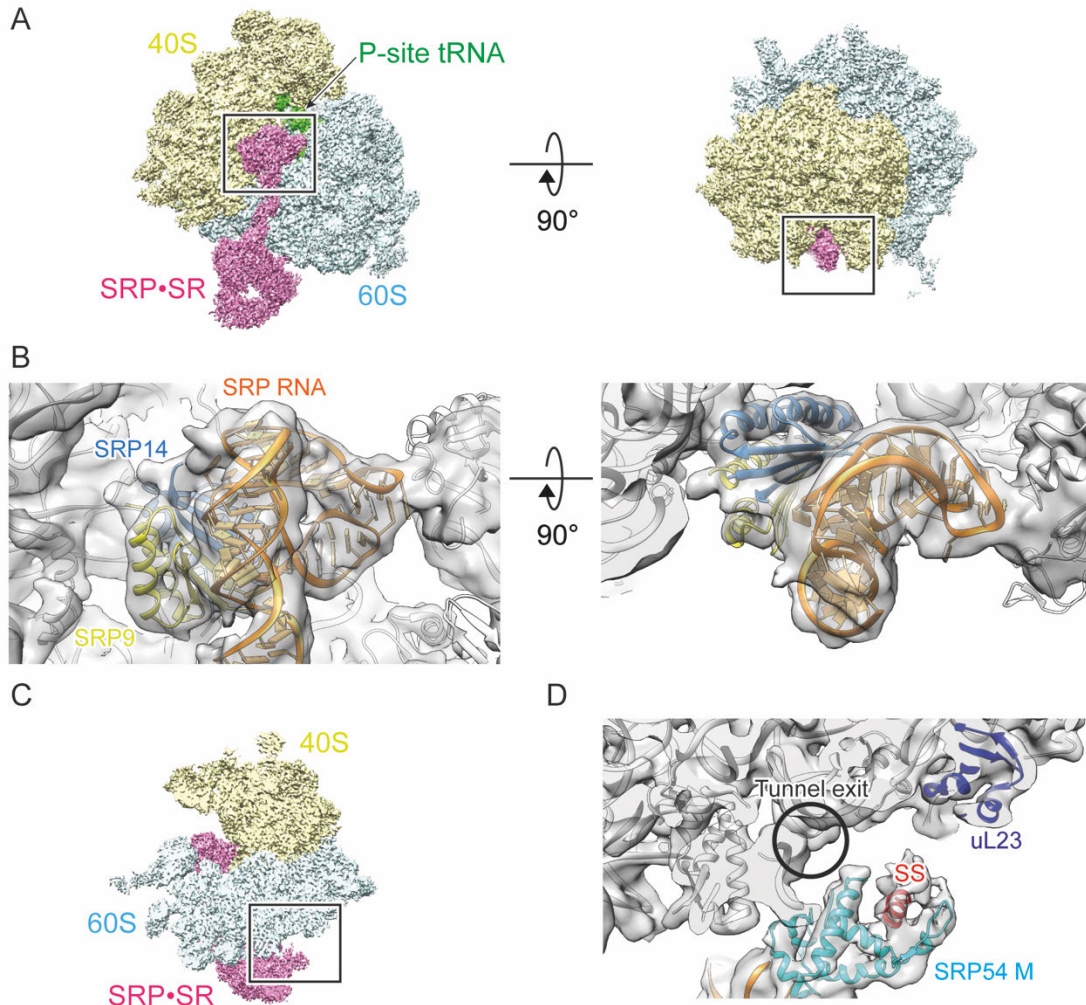


**Fig. S3. The map and structure model of SRP Alu domain and ribosomal tunnel exit.**

(A) The map of SRP-SR-RNC complex low-pass filtered to 3.7 Å resolution is shown and colored as in Fig. 1A from two perpendicular directions. The P-site tRNA is colored green. The Alu domain region of SRP highlighted by a square is shown in (B). (B) Structure model of SRP Alu domain bound to the ribosome fitted into the map from two perpendicular directions. The ribosome model is from the previous study (PDB ID: 3JAJ) (27). The map low-pass filtered to 6 Å resolution is colored gray. Models are shown and colored as in Fig. 1B. SRP9 and SRP14 are colored yellow and blue, respectively. (C) Same as (A) but from the different direction. The ribosomal tunnel exit region highlighted by a square is shown in (D). (D) Structure model of ribosomal tunnel exit region. The models are shown and colored as in Fig. 1B. The ribosomal protein uL23 is colored blue. The map is shown as in (B). The ribosomal tunnel exit is indicated by a circle.

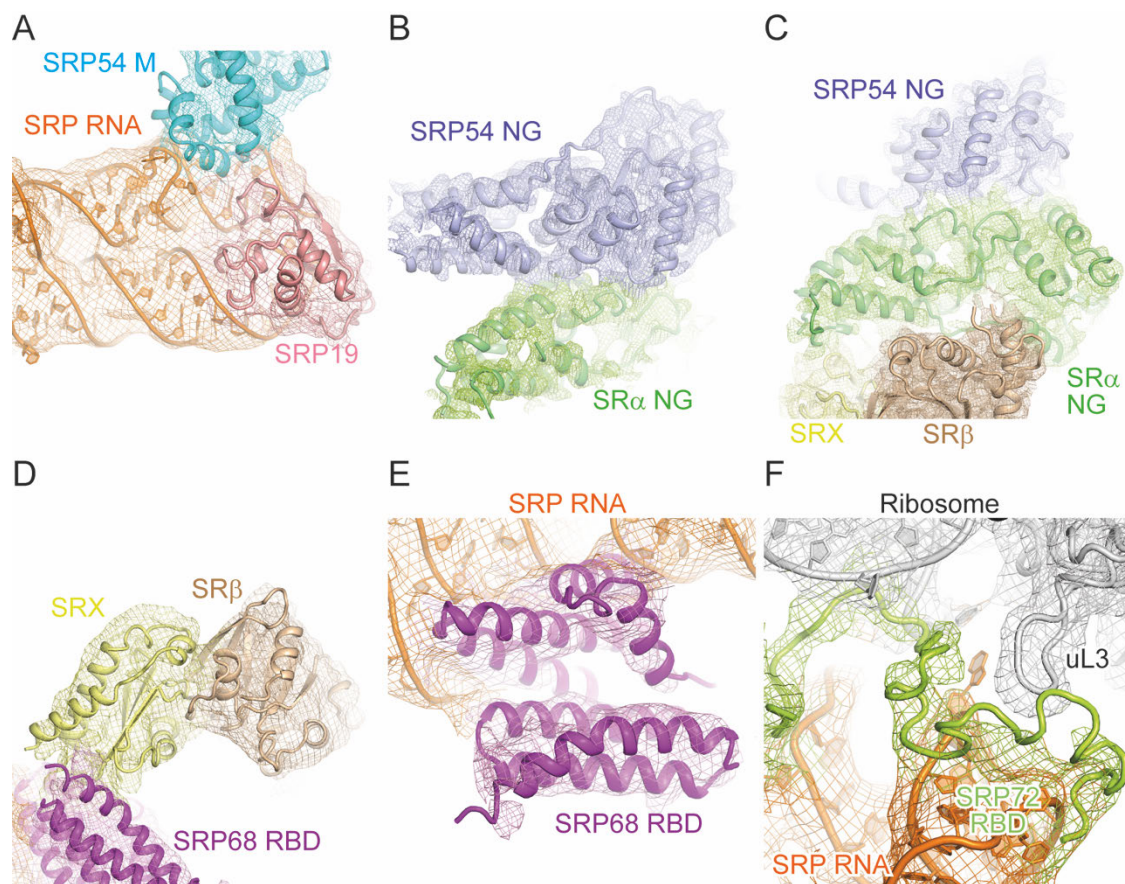


**Fig. S4. Models and maps of SRP and SR components in the S domain.**

(A-F) Models of SRP and SR components fitted into the map. Models are shown in cartoon and colored as in Fig. 1C. In (B) and (C), the map low-pass filtered to 4.5 Å resolution is shown. In the other panels, the map low-pass filtered to 6 Å resolution is shown. SRP68 RBD is shown in the higher threshold.

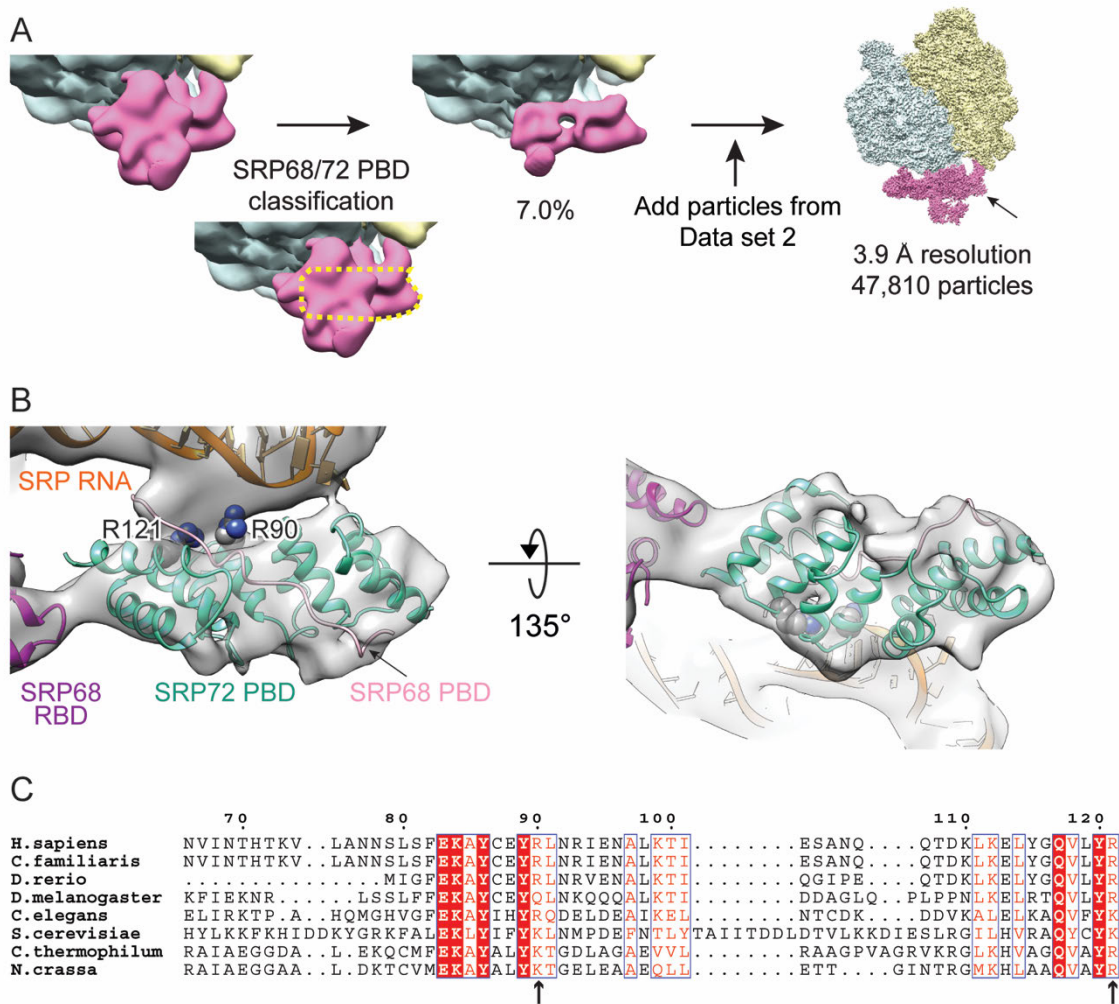


**Fig. S5. SRP68/72 PBD attached to SRP RNA.**

(A) The focused classification scheme of the data set 1 for the SRP68/72 PBD from the 9.8% particles after the 2nd classification (Fig. S1). The shape of the mask used for the local 3D classification is represented as the dashed yellow line. Ribosomal particles from data set 2, classified in the same procedure, were combined with data set 1 before the final refinement step. The density of SRP68/72 PBD is pointed by the arrow. See Materials and Methods for details. (B) The model of SRP68/72 PBD (PDB ID: 5M72) (22) was tentatively fitted into the map and is shown from two perpendicular directions. The map low-pass filtered to 8 Å resolution is colored gray. Models are colored as in Fig. 1B. Arg90 and Arg121 of SRP72 are shown in spheres. (C) Part of the sequence alignment of SRP72 prepared as described (22). Arg90 and Arg121 are pointed by arrows.

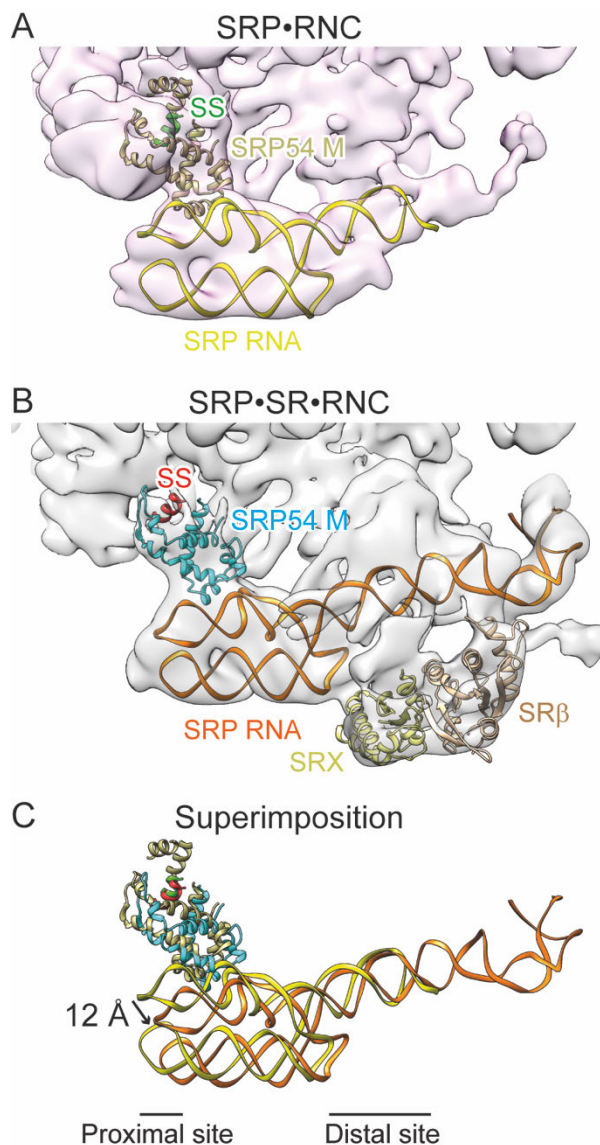


**Fig. S6. Structural comparison of SRP RNA and the signal sequence-bound SRP54 M domain between SRP·RNC and SRP·SR·RNC complexes.**  
**(A)** Structure model and map of SRP RNA in SRP·RNC complex (PDB ID: 3JAJ, EMD-3037) (27). The SRP RNA, SRP54 M domain, and signal sequence is colored yellow, dark khaki, and green, respectively. The map low-pass filtered to 10 Å resolution is colored pink. **(B)** Structure model and map of SRP RNA in SRP·SR·RNC complex (this study). Models are colored as in Fig. 1B. The map low-pass filtered to 10 Å resolution is colored gray. The model of SRX·SRβ is shown and colored as in Fig. 1B. **(C)** Structural comparison of SRP RNA between SRP·RNC and SRP·SR·RNC complexes. Superimposition of the two structures indicates a displacement of ~12 Å in the SRP RNA at the proximal site, shown as an arrow.

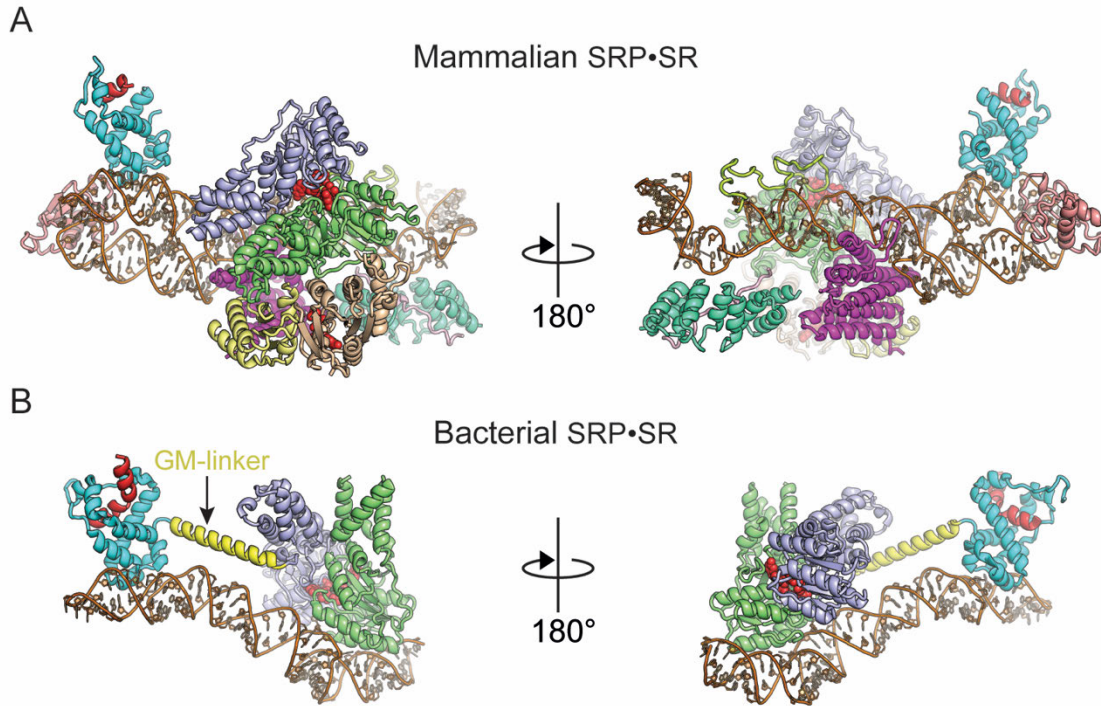


**Fig. S7. Structural comparison of the mammalian SRP•SR•GMPPNP with bacterial SRP•SR•GDP•AlF<sub>4</sub> on RNC.**

SRP and SR components and GMPPNP or GDP•AlF<sub>4</sub> molecules are shown as in Fig. 1C, except that SRP RNA is shown in the cartoon. **(A)** Mammalian SRP•SR•GMPPNP structure from two opposite directions (this study). **(B)** Bacterial SRP•SR•GDP•AlF<sub>4</sub> structure from two opposite directions (PDB ID: 5NCO) (29). The GM-linker connecting the NG and M domains of Ffh (bacterial SRP54) is colored yellow.

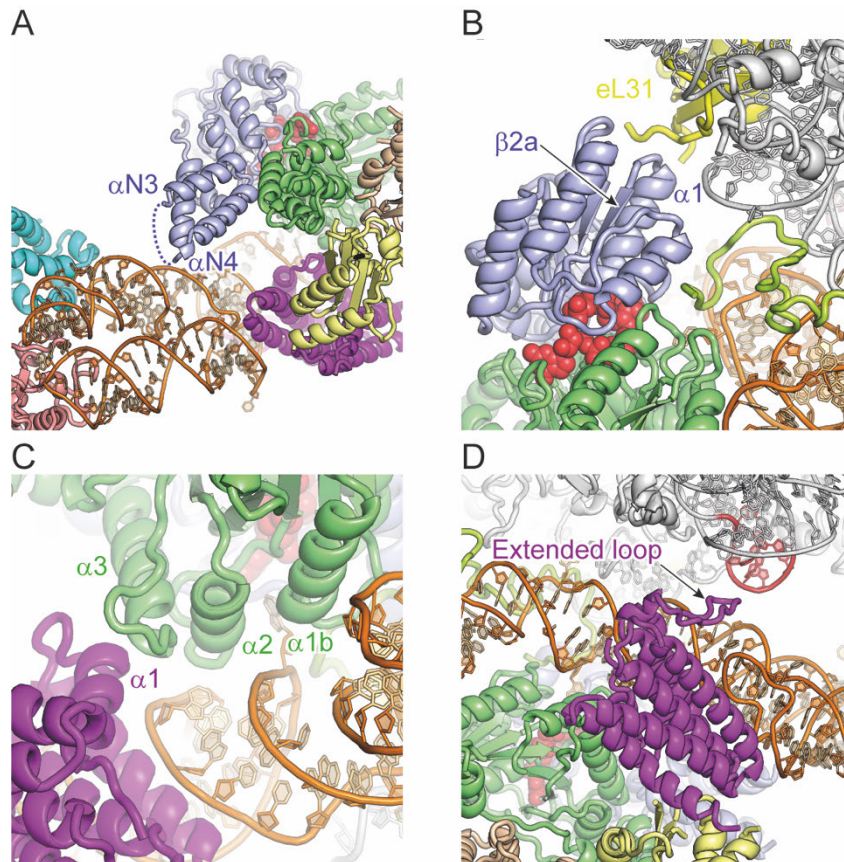


**Fig. S8. Intermolecular interactions between the ribosome, NG heterodimer, SRP RNA, and SRP68 RBD at the SRP RNA distal site.**

(A-D) The ribosome, SRP, and SR components are shown as in Fig. S4. GMPPNP molecules bound to the NG heterodimer are shown in the red spheres. The disordered loop between  $\alpha N3$  and  $\alpha N4$  of the SRP54 NG domain is shown as the dashed line. The ribosomal protein eL31 is colored yellow. SRP68/72 PBD is not shown for clarity. Secondary structure elements of proteins and the SRP68 RBD extended loop are labeled. The 28S rRNA region contacting SRP68 RBD extended loop is colored red.

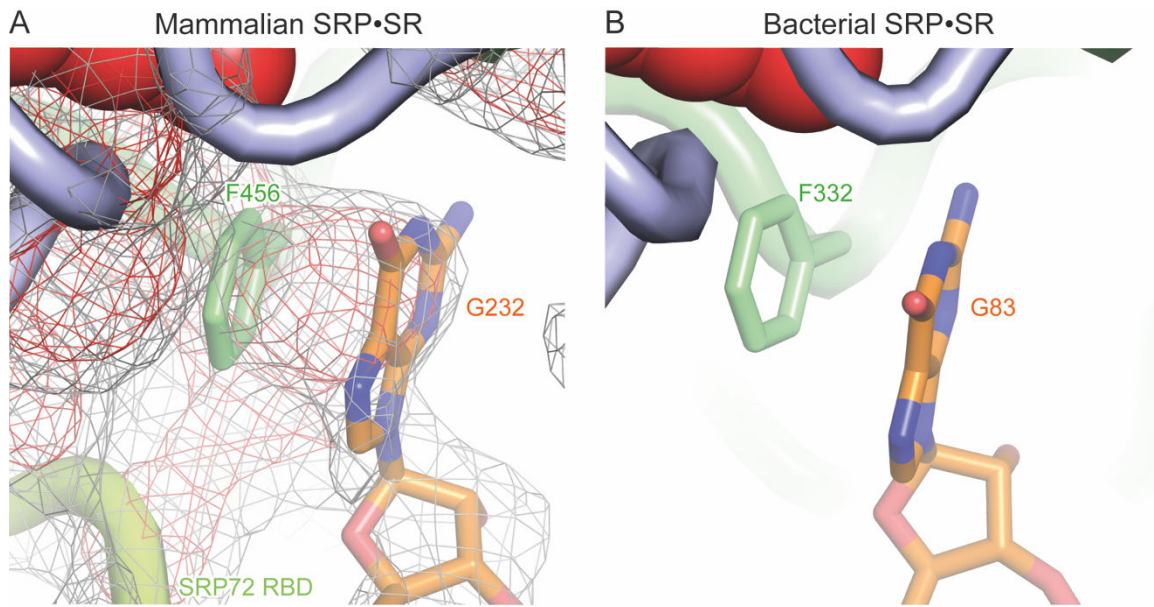


**Fig. S9. The conserved stacking interaction between the guanine base of SRP RNA and the phenylalanine residue of SR.**

(A) The stacking interaction between SRP RNA G232 and SR $\alpha$  Phe456 in mammalian SRP•SR•RNC complex (this study). The model is shown as in Fig. 1C but the SRP RNA G232 is shown in the stick model colored orange. The side chain of SR $\alpha$  Phe456 is also shown in the stick model. The map low-pass filtered to 4.5 Å resolution is shown as mesh at the two contour levels (gray and red ). (B) Stacking interaction between SRP RNA G83 and FtsY (bacterial SR $\alpha$ ) Phe332 in bacterial SRP•SR•RNC complex shown as in (A) (PDB ID: 5NCO) (29). G83 of SRP RNA is colored orange.

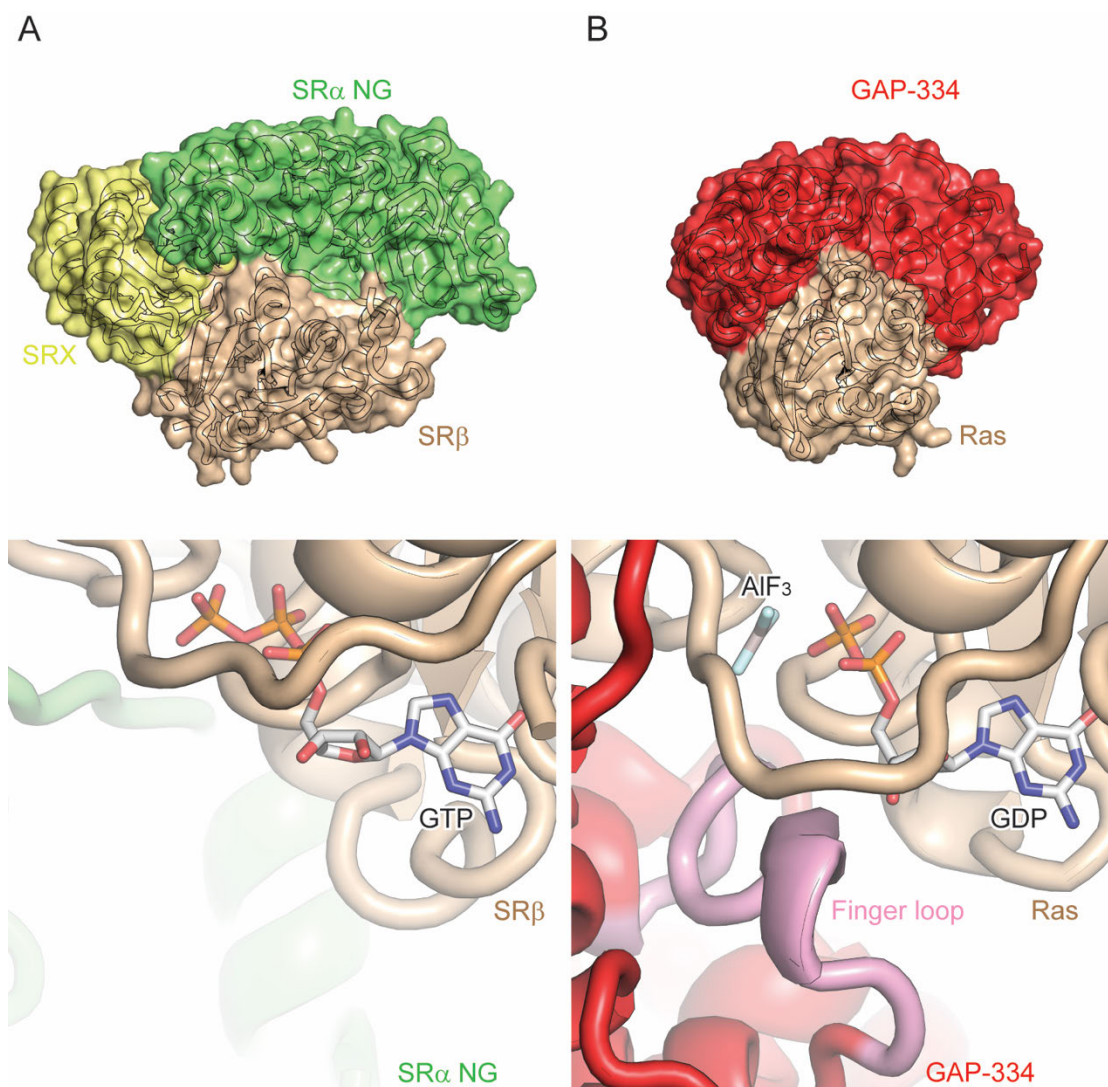


**Fig. S10. Structural comparison of SR $\beta$  in mammalian SRP·SR·RNC complex with Ras in complex with GAP-334.**

(A) Surface and cartoon representation of SR $\beta$  bound to SRX and SR $\alpha$  NG domain at the SRP RNA distal site (top) and the close-up view of the GTP binding site of SR $\beta$  (bottom) (this study). The model is shown and colored as in Fig. 1C and the GTP molecule is shown in the stick model. (B) Surface and cartoon representation of Ras bound to GAP-334 (top) and the close-up view of the GTP binding site of Ras (bottom) (PDB ID: 1WQ1) (35). Models of Ras and GAP-334 are colored wheat and red, respectively. The GTPase catalytic finger loop of GAP-334 is colored pink, and GDP and AIF<sub>3</sub> molecules are shown in the stick model.

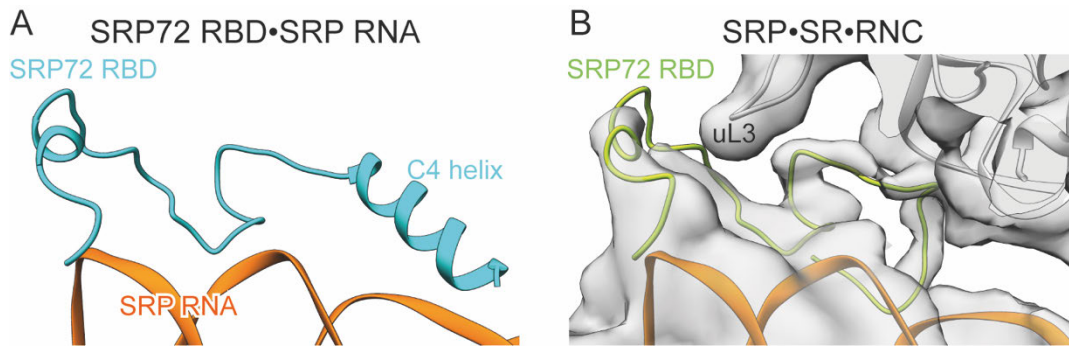


**Fig. S11. Structural comparison of SRP RNA-bound SRP72 RBD in the isolated form and SRP·SR·RNC complex.**

(A) Structure model of SRP72 RBD bound to SRP RNA (PDB ID: 5M73) (22). SRP RNA and SRP72 RBD are shown in the cartoon colored orange and cyan, respectively.

(B) Structure model and map of SRP72 RBD in SRP·SR·RNC complex (this study).

Models are shown and colored as in Fig. 1B. The map low-pass filtered to 6 Å resolution is colored gray.

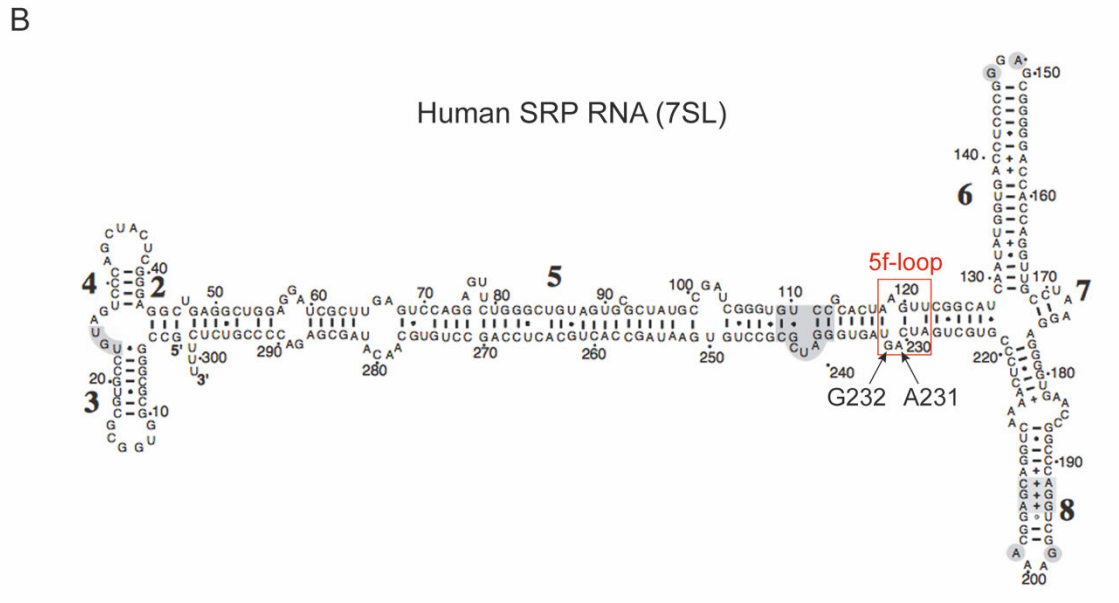
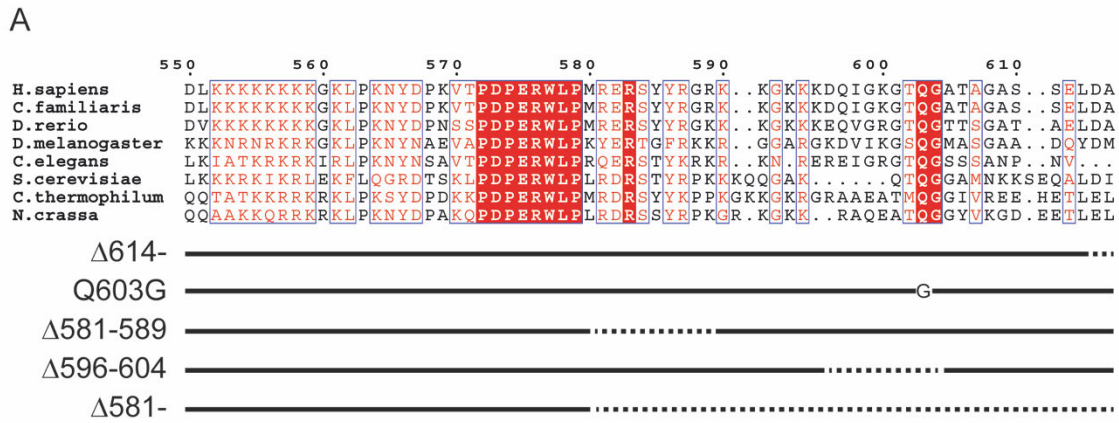


**Fig. S12. Design of SRP variants.**  
 (A) Sequence alignment of SRP72 C-terminal region (550-615, human numbering) prepared as in Fig. S5C (top) and the schematic diagram of designed human SRP72 (h72) variants (bottom). Note that this sequence alignment does not cover the whole C-terminal region of SRP72 (h72 has 671 residues.). (B) Secondary structure of human SRP RNA (7SL) (64). The 5f-loop is indicated by the red square, and A231 and G232 are pointed by arrows.

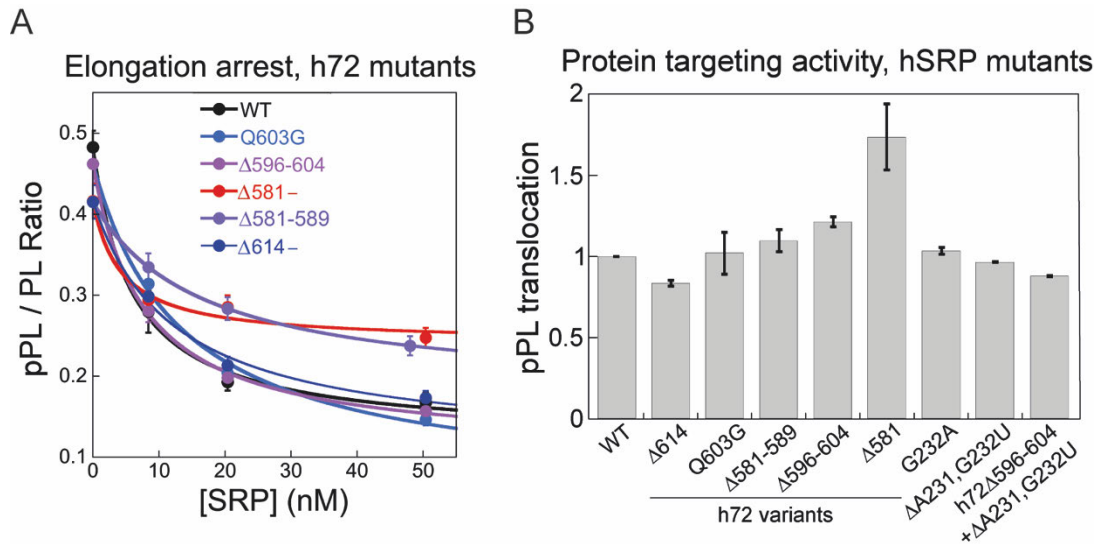


**Fig. S13. Translation arrest and membrane targeting efficiencies of SRP variants.**

(A) Translation arrest activities of wildtype and mutant SRPs were measured in wheat germ lysate as described in the Materials and Methods. The SRP concentration dependences of translational suppression of preprolactin (pPL) also provides a measure for the binding of SRP to RNCs bearing the pPL nascent chain. Data were reported as mean  $\pm$ S.D., with  $n = 2$ . (B) Translocation efficiencies of pPL by human SRPs bearing indicated SRP72 mutations and/or SRP RNA mutations. All measurements contained 6 nM of respective SRPs, SR $\alpha\beta\Delta$ TM, and 0.2 eq/ $\mu$ L salt-washed/trypsinized rough ER microsomes (TKRM). Translocation efficiencies were normalized to that of wildtype SRP. Data were reported as mean  $\pm$ S.D., with  $n = 2-4$ .

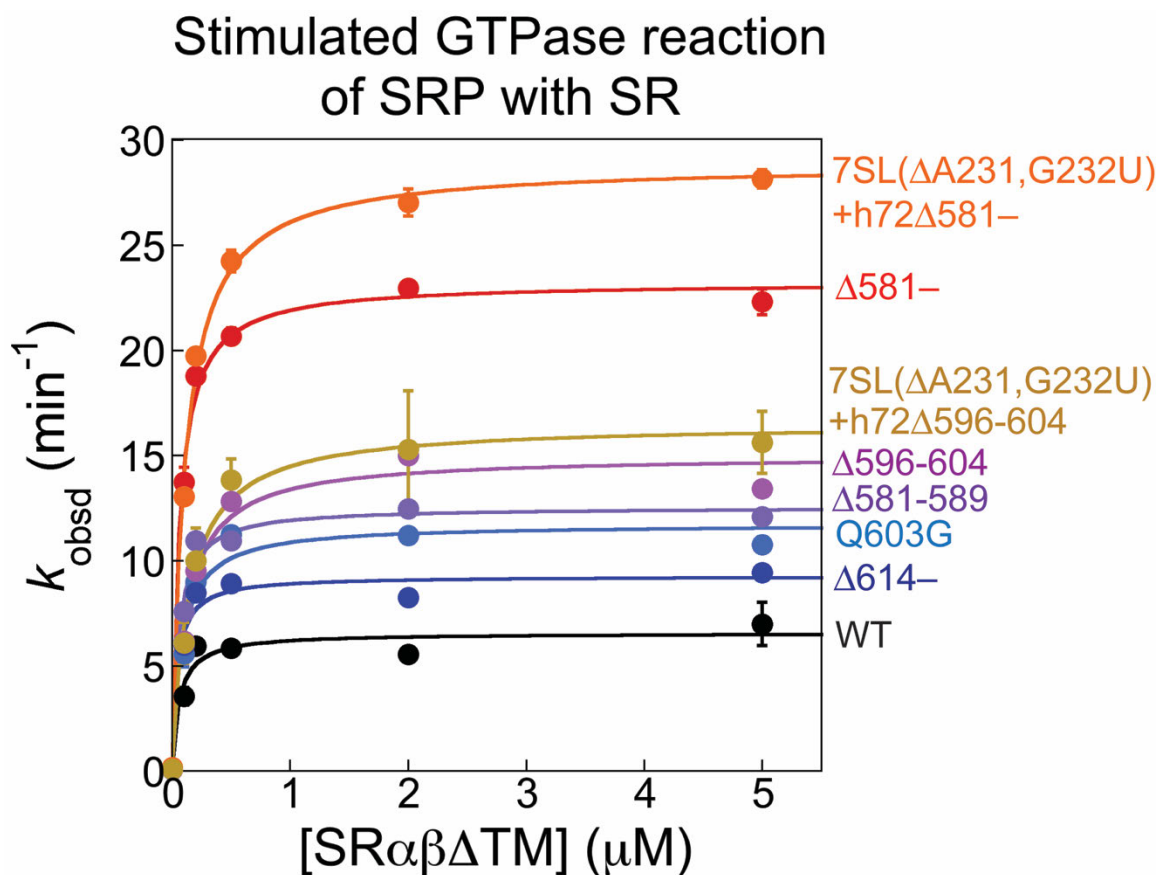


**Fig. S14. Reciprocally stimulated GTPase reactions of SRP with SR.**

The GTPase activity was measured as described in the Materials and Methods. All reactions contained 200 nM wild type or mutant SRP fused to the signal sequence, indicated concentrations of SRαβΔTM, 250 nM 80S ribosome, and 100 μM GTP doped with  $\gamma$ - $^{32}\text{P}$ -GTP. The lines are fits of the data to the Michaelis-Menten equation, which gave the values of  $k_{\text{cat}}$  reported in Fig. 3C and 3D. Data were reported as mean  $\pm$  S.D., with  $n = 3-6$ .

**Table S1. Data collection, structure model refinement, and validation statistics**

| <b>Data Collection</b>                      | <b>SRP·SR·60S (SRP·SR)</b> |
|---|----------------------------|
| Number of particles                         | 45,800                     |
| Voltage (kV)                                | 300                        |
| Defocus range ( $\mu\text{m}$ )             | 1.2-3.0                    |
| Pixel size ( $\text{\AA}$ )                 | 1.39                       |
| Electron dose ( $\text{e}^-/\text{\AA}^2$ ) | 40                         |
| <b>Structure model refinement</b>           |                            |
| Resolution ( $\text{\AA}$ )                 | 3.7 (6.6)                  |
| Map sharpening B-factor ( $\text{\AA}^2$ )  | -204                       |
| Average B-factor ( $\text{\AA}^2$ )         | 82.9                       |
| r.m.s. deviations                           |                            |
| Bond length ( $\text{\AA}$ )                | 0.006                      |
| Bond angles ( $^\circ$ )                    | 1.050                      |
| <b>Validation statistics</b>                |                            |
| Molprobit Score                             | 3.2 (2.7)                  |
| Clashscore, all atoms                       | 15.8 (15.3)                |
| <b>Protein</b>                              |                            |
| Favored rotamers (%)                        | 68.5 (85.3)                |
| Ramachandran plot                           |                            |
| Favored (%)                                 | 88.6 (95.0)                |
| Allowed (%)                                 | 99.4 (99.8)                |
| Outliers (%)                                | 0.6 (0.2)                  |
| <b>RNA</b>                                  |                            |
| Correct sugar puckers (%)                   | 95.4 (95.7)                |
| Good backbone conformations (%)             | 67.1 (72.7)                |

## References

1. P. Walter, G. Blobel, Purification of a membrane-associated protein complex required for protein translocation across the endoplasmic reticulum. *Proc. Natl. Acad. Sci. U.S.A.* **77**, 7112–7116 (1980). doi:10.1073/pnas.77.12.7112 [Medline](#)
2. R. Gilmore, P. Walter, G. Blobel, Protein translocation across the endoplasmic reticulum. II. Isolation and characterization of the signal recognition particle receptor. *J. Cell Biol.* **95**, 470–477 (1982). doi:10.1083/jcb.95.2.470 [Medline](#)
3. D. I. Meyer, E. Krause, B. Dobberstein, Secretory protein translocation across membranes—the role of the 'docking protein'. *Nature* **297**, 647–650 (1982). doi:10.1038/297647a0 [Medline](#)
4. J. W. Chartron, K. C. L. Hunt, J. Frydman, Cotranslational signal-independent SRP preloading during membrane targeting. *Nature* **536**, 224–228 (2016). doi:10.1038/nature19309 [Medline](#)
5. P. Walter, I. Ibrahimi, G. Blobel, Translocation of proteins across the endoplasmic reticulum. I. Signal recognition protein (SRP) binds to in-vitro-assembled polysomes synthesizing secretory protein. *J. Cell Biol.* **91**, 545–550 (1981). doi:10.1083/jcb.91.2.545 [Medline](#)
6. U. C. Krieg, P. Walter, A. E. Johnson, Photocrosslinking of the signal sequence of nascent preprolactin to the 54-kilodalton polypeptide of the signal recognition particle. *Proc. Natl. Acad. Sci. U.S.A.* **83**, 8604–8608 (1986). doi:10.1073/pnas.83.22.8604 [Medline](#)
7. S. M. Simon, G. Blobel, A protein-conducting channel in the endoplasmic reticulum. *Cell* **65**, 371–380 (1991). doi:10.1016/0092-8674(91)90455-8 [Medline](#)
8. R. M. Voorhees, R. S. Hegde, Toward a structural understanding of co-translational protein translocation. *Curr. Opin. Cell Biol.* **41**, 91–99 (2016). doi:10.1016/j.ceb.2016.04.009 [Medline](#)
9. Y. Nyathi, B. M. Wilkinson, M. R. Pool, Co-translational targeting and translocation of proteins to the endoplasmic reticulum. *Biochim. Biophys. Acta* **1833**, 2392–2402 (2013). doi:10.1016/j.bbamer.2013.02.021 [Medline](#)
10. E. C. Mandon, S. F. Trueman, R. Gilmore, Protein translocation across the rough endoplasmic reticulum. *Cold Spring Harb. Perspect. Biol.* **5**, a013342 (2013). doi:10.1101/cshperspect.a013342 [Medline](#)
11. P. Walter, G. Blobel, Signal recognition particle contains a 7S RNA essential for protein translocation across the endoplasmic reticulum. *Nature* **299**, 691–698 (1982). doi:10.1038/299691a0 [Medline](#)
12. M. Halic, T. Becker, M. R. Pool, C. M. T. Spahn, R. A. Grassucci, J. Frank, R. Beckmann, Structure of the signal recognition particle interacting with the elongation-arrested ribosome. *Nature* **427**, 808–814 (2004). doi:10.1038/nature02342 [Medline](#)
13. H. Lütcke, S. High, K. Römisch, A. J. Ashford, B. Dobberstein, The methionine-rich domain of the 54 kDa subunit of signal recognition particle is sufficient for the interaction with signal sequences. *EMBO J.* **11**, 1543–1551 (1992). [Medline](#)

14. J. D. Miller, S. Tajima, L. Lauffer, P. Walter, The beta subunit of the signal recognition particle receptor is a transmembrane GTPase that anchors the alpha subunit, a peripheral membrane GTPase, to the endoplasmic reticulum membrane. *J. Cell Biol.* **128**, 273–282 (1995). [doi:10.1083/jcb.128.3.273](https://doi.org/10.1083/jcb.128.3.273) [Medline](#)
15. S. Tajima, L. Lauffer, V. L. Rath, P. Walter, The signal recognition particle receptor is a complex that contains two distinct polypeptide chains. *J. Cell Biol.* **103**, 1167–1178 (1986). [doi:10.1083/jcb.103.4.1167](https://doi.org/10.1083/jcb.103.4.1167) [Medline](#)
16. J. C. Young, J. Ursini, K. R. Legate, J. D. Miller, P. Walter, D. W. Andrews, An amino-terminal domain containing hydrophobic and hydrophilic sequences binds the signal recognition particle receptor  $\alpha$  subunit to the  $\beta$  subunit on the endoplasmic reticulum membrane. *J. Biol. Chem.* **270**, 15650–15657 (1995). [doi:10.1074/jbc.270.26.15650](https://doi.org/10.1074/jbc.270.26.15650) [Medline](#)
17. P. J. Rapiejko, R. Gilmore, Empty site forms of the SRP54 and SR alpha GTPases mediate targeting of ribosome-nascent chain complexes to the endoplasmic reticulum. *Cell* **89**, 703–713 (1997). [doi:10.1016/S0092-8674\(00\)80253-6](https://doi.org/10.1016/S0092-8674(00)80253-6) [Medline](#)
18. K. Wild, G. Bange, D. Motiejunas, J. Kribelbauer, A. Hendricks, B. Segnitz, R. C. Wade, I. Sinning, Structural Basis for Conserved Regulation and Adaptation of the Signal Recognition Particle Targeting Complex. *J. Mol. Biol.* **428**, 2880–2897 (2016). [doi:10.1016/j.jmb.2016.05.015](https://doi.org/10.1016/j.jmb.2016.05.015) [Medline](#)
19. S. F. Ataide, N. Schmitz, K. Shen, A. Ke, S. O. Shan, J. A. Doudna, N. Ban, The crystal structure of the signal recognition particle in complex with its receptor. *Science* **331**, 881–886 (2011). [doi:10.1126/science.1196473](https://doi.org/10.1126/science.1196473) [Medline](#)
20. K. Shen, S. Arslan, D. Akopian, T. Ha, S. O. Shan, Activated GTPase movement on an RNA scaffold drives co-translational protein targeting. *Nature* **492**, 271–275 (2012). [doi:10.1038/nature11726](https://doi.org/10.1038/nature11726) [Medline](#)
21. M. Halic, M. Gartmann, O. Schlenker, T. Mielke, M. R. Pool, I. Sinning, R. Beckmann, Signal recognition particle receptor exposes the ribosomal translocon binding site. *Science* **312**, 745–747 (2006). [doi:10.1126/science.1124864](https://doi.org/10.1126/science.1124864) [Medline](#)
22. M. M. M. Becker, K. Lapouge, B. Segnitz, K. Wild, I. Sinning, Structures of human SRP72 complexes provide insights into SRP RNA remodeling and ribosome interaction. *Nucleic Acids Res.* **45**, 470–481 (2017). [doi:10.1093/nar/gkw1124](https://doi.org/10.1093/nar/gkw1124) [Medline](#)
23. V. Siegel, P. Walter, Each of the activities of signal recognition particle (SRP) is contained within a distinct domain: Analysis of biochemical mutants of SRP. *Cell* **52**, 39–49 (1988). [doi:10.1016/0092-8674\(88\)90529-6](https://doi.org/10.1016/0092-8674(88)90529-6) [Medline](#)
24. E. C. Mandon, Y. Jiang, R. Gilmore, Dual recognition of the ribosome and the signal recognition particle by the SRP receptor during protein targeting to the endoplasmic reticulum. *J. Cell Biol.* **162**, 575–585 (2003). [doi:10.1083/jcb.200303143](https://doi.org/10.1083/jcb.200303143) [Medline](#)
25. G. Bacher, M. Pool, B. Dobberstein, The ribosome regulates the GTPase of the  $\beta$ -subunit of the signal recognition particle receptor. *J. Cell Biol.* **146**, 723–730 (1999). [doi:10.1083/jcb.146.4.723](https://doi.org/10.1083/jcb.146.4.723) [Medline](#)

26. T. A. Fulga, I. Sinning, B. Dobberstein, M. R. Pool, SR $\beta$  coordinates signal sequence release from SRP with ribosome binding to the translocon. *EMBO J.* **20**, 2338–2347 (2001). doi:10.1093/emboj/20.9.2338 [Medline](#)
27. R. M. Voorhees, R. S. Hegde, Structures of the scanning and engaged states of the mammalian SRP-ribosome complex. *eLife* **4**, e07975 (2015). doi:10.7554/eLife.07975 [Medline](#)
28. A. Jomaa, D. Boehringer, M. Leibundgut, N. Ban, Structures of the E. coli translating ribosome with SRP and its receptor and with the translocon. *Nat. Commun.* **7**, 10471 (2016). doi:10.1038/ncomms10471 [Medline](#)
29. A. Jomaa, Y.-H. H. Fu, D. Boehringer, M. Leibundgut, S. O. Shan, N. Ban, Structure of the quaternary complex between SRP, SR, and translocon bound to the translating ribosome. *Nat. Commun.* **8**, 15470 (2017). doi:10.1038/ncomms15470 [Medline](#)
30. O. Schlenker, A. Hendricks, I. Sinning, K. Wild, The structure of the mammalian signal recognition particle (SRP) receptor as prototype for the interaction of small GTPases with Longin domains. *J. Biol. Chem.* **281**, 8898–8906 (2006). doi:10.1074/jbc.M512415200 [Medline](#)
31. J. T. Grotwinkel, K. Wild, B. Segnitz, I. Sinning, SRP RNA remodeling by SRP68 explains its role in protein translocation. *Science* **344**, 101–104 (2014). doi:10.1126/science.1249094 [Medline](#)
32. F. Voigts-Hoffmann, N. Schmitz, K. Shen, S. O. Shan, S. F. Ataide, N. Ban, The structural basis of FtsY recruitment and GTPase activation by SRP RNA. *Mol. Cell* **52**, 643–654 (2013). doi:10.1016/j.molcel.2013.10.005 [Medline](#)
33. K. R. Legate, D. Falcone, D. W. Andrews, Nucleotide-dependent binding of the GTPase domain of the signal recognition particle receptor  $\beta$ -subunit to the  $\alpha$ -subunit. *J. Biol. Chem.* **275**, 27439–27446 (2000). [Medline](#)
34. T. Schwartz, G. Blobel, Structural basis for the function of the  $\beta$  subunit of the eukaryotic signal recognition particle receptor. *Cell* **112**, 793–803 (2003). doi:10.1016/S0092-8674(03)00161-2 [Medline](#)
35. K. Scheffzek, M. R. Ahmadian, W. Kabsch, L. Wiesmüller, A. Lautwein, F. Schmitz, A. Wittinghofer, The Ras-RasGAP complex: Structural basis for GTPase activation and its loss in oncogenic Ras mutants. *Science* **277**, 333–338 (1997). doi:10.1126/science.277.5324.333 [Medline](#)
36. P. J. Utz, M. Hottelet, T. M. Le, S. J. Kim, M. E. Geiger, W. J. van Venrooij, P. Anderson, The 72-kDa component of signal recognition particle is cleaved during apoptosis. *J. Biol. Chem.* **273**, 35362–35370 (1998). doi:10.1074/jbc.273.52.35362 [Medline](#)
37. Z. Cheng, R. Gilmore, Slow translocon gating causes cytosolic exposure of transmembrane and luminal domains during membrane protein integration. *Nat. Struct. Mol. Biol.* **13**, 930–936 (2006). doi:10.1038/nsmb1146 [Medline](#)
38. G. Bacher, H. Lütcke, B. Jungnickel, T. A. Rapoport, B. Dobberstein, Regulation by the ribosome of the GTPase of the signal-recognition particle during protein targeting. *Nature* **381**, 248–251 (1996). doi:10.1038/381248a0 [Medline](#)

39. D. Görlich, T. A. Rapoport, Protein translocation into proteoliposomes reconstituted from purified components of the endoplasmic reticulum membrane. *Cell* **75**, 615–630 (1993). doi:10.1016/0092-8674(93)90483-7 [Medline](#)
40. S. Q. Zheng, E. Palovcak, J.-P. Armache, K. A. Verba, Y. Cheng, D. A. Agard, MotionCor2: Anisotropic correction of beam-induced motion for improved cryo-electron microscopy. *Nat. Methods* **14**, 331–332 (2017). doi:10.1038/nmeth.4193 [Medline](#)
41. A. Rohou, N. Grigorieff, CTFFIND4: Fast and accurate defocus estimation from electron micrographs. *J. Struct. Biol.* **192**, 216–221 (2015). doi:10.1016/j.jsb.2015.08.008 [Medline](#)
42. S. J. Ludtke, P. R. Baldwin, W. Chiu, EMAN: Semiautomated software for high-resolution single-particle reconstructions. *J. Struct. Biol.* **128**, 82–97 (1999). doi:10.1006/jsbi.1999.4174 [Medline](#)
43. D. Kimanius, B. O. Forsberg, S. H. W. Scheres, E. Lindahl, Accelerated cryo-EM structure determination with parallelisation using GPUs in RELION-2. *eLife* **5**, e18722 (2016). doi:10.7554/eLife.18722 [Medline](#)
44. S. H. W. Scheres, RELION: Implementation of a Bayesian approach to cryo-EM structure determination. *J. Struct. Biol.* **180**, 519–530 (2012). doi:10.1016/j.jsb.2012.09.006 [Medline](#)
45. T. V. Budkevich, J. Giesebrecht, E. Behrmann, J. Loerke, D. J. F. Ramrath, T. Mielke, J. Ismer, P. W. Hildebrand, C.-S. Tung, K. H. Nierhaus, K. Y. Sanbonmatsu, C. M. T. Spahn, Regulation of the mammalian elongation cycle by subunit rolling: A eukaryotic-specific ribosome rearrangement. *Cell* **158**, 121–131 (2014). doi:10.1016/j.cell.2014.04.044 [Medline](#)
46. X. C. Bai, E. Rajendra, G. Yang, Y. Shi, S. H. Scheres, Sampling the conformational space of the catalytic subunit of human  $\gamma$ -secretase. *eLife* **4**, e11182 (2015). doi:10.7554/eLife.11182 [Medline](#)
47. K. Zhang, Gctf: Real-time CTF determination and correction. *J. Struct. Biol.* **193**, 1–12 (2016). doi:10.1016/j.jsb.2015.11.003 [Medline](#)
48. J. B. Heymann, D. M. Belnap, Bsoft: Image processing and molecular modeling for electron microscopy. *J. Struct. Biol.* **157**, 3–18 (2007). doi:10.1016/j.jsb.2006.06.006 [Medline](#)
49. G. Cardone, J. B. Heymann, A. C. Steven, One number does not fit all: Mapping local variations in resolution in cryo-EM reconstructions. *J. Struct. Biol.* **184**, 226–236 (2013). doi:10.1016/j.jsb.2013.08.002 [Medline](#)
50. E. F. Pettersen, T. D. Goddard, C. C. Huang, G. S. Couch, D. M. Greenblatt, E. C. Meng, T. E. Ferrin, UCSF Chimera—a visualization system for exploratory research and analysis. *J. Comput. Chem.* **25**, 1605–1612 (2004). doi:10.1002/jcc.20084 [Medline](#)
51. P. Emsley, K. Cowtan, Coot: Model-building tools for molecular graphics. *Acta Crystallogr. D Biol. Crystallogr.* **60**, 2126–2132 (2004). doi:10.1107/S0907444904019158 [Medline](#)
52. A. Kuglstatter, C. Oubridge, K. Nagai, Induced structural changes of 7SL RNA during the assembly of human signal recognition particle. *Nat. Struct. Biol.* **9**, 740–744 (2002). doi:10.1038/nsb843 [Medline](#)

53. B. Beckert, A. Kedrov, D. Sohmen, G. Kempf, K. Wild, I. Sinning, H. Stahlberg, D. N. Wilson, R. Beckmann, Translational arrest by a prokaryotic signal recognition particle is mediated by RNA interactions. *Nat. Struct. Mol. Biol.* **22**, 767–773 (2015). doi:10.1038/nsmb.3086 [Medline](#)
54. B. J. Greber, D. Boehringer, M. Leibundgut, P. Bieri, A. Leitner, N. Schmitz, R. Aebersold, N. Ban, The complete structure of the large subunit of the mammalian mitochondrial ribosome. *Nature* **515**, 283–286 (2014). doi:10.1038/nature13895 [Medline](#)
55. P. D. Adams, P. V. Afonine, G. Bunkóczi, V. B. Chen, I. W. Davis, N. Echols, J. J. Headd, L.-W. Hung, G. J. Kapral, R. W. Grosse-Kunstleve, A. J. McCoy, N. W. Moriarty, R. Oeffner, R. J. Read, D. C. Richardson, J. S. Richardson, T. C. Terwilliger, P. H. Zwart, PHENIX: A comprehensive Python-based system for macromolecular structure solution. *Acta Crystallogr. D Biol. Crystallogr.* **66**, 213–221 (2010). doi:10.1107/S09074444909052925 [Medline](#)
56. F. Bovia, N. Wolff, S. Ryser, K. Strub, The SRP9/14 subunit of the human signal recognition particle binds to a variety of Alu-like RNAs and with higher affinity than its mouse homolog. *Nucleic Acids Res.* **25**, 318–325 (1997). doi:10.1093/nar/25.2.318 [Medline](#)
57. K. Gowda, S. D. Black, I. Moeller, Y. Sakakibara, M.-C. Liu, C. Zwieb, Protein SRP54 of human signal recognition particle: Cloning, expression, and comparative analysis of functional sites. *Gene* **207**, 197–207 (1998). doi:10.1016/S0378-1119(97)00627-6 [Medline](#)
58. K. A. Henry, C. Zwieb, H. M. Fried, Purification and biochemical characterization of the 19-kDa signal recognition particle RNA-binding protein expressed as a hexahistidine-tagged polypeptide in *Escherichia coli*. *Protein Expr. Purif.* **9**, 15–26 (1997). doi:10.1006/prev.1996.0667 [Medline](#)
59. E. Menichelli, C. Isel, C. Oubridge, K. Nagai, Protein-induced conformational changes of RNA during the assembly of human signal recognition particle. *J. Mol. Biol.* **367**, 187–203 (2007). doi:10.1016/j.jmb.2006.12.056 [Medline](#)
60. S. O. Shan, S. Chandrasekar, P. Walter, Conformational changes in the GTPase modules of the signal reception particle and its receptor drive initiation of protein translocation. *J. Cell Biol.* **178**, 611–620 (2007). doi:10.1083/jcb.200702018 [Medline](#)
61. T. Powers, P. Walter, Co-translational protein targeting catalyzed by the *Escherichia coli* signal recognition particle and its receptor. *EMBO J.* **16**, 4880–4886 (1997). doi:10.1093/emboj/16.16.4880 [Medline](#)
62. P. Peluso, S. O. Shan, S. Nock, D. Herschlag, P. Walter, Role of SRP RNA in the GTPase cycles of Ffh and FtsY. *Biochemistry* **40**, 15224–15233 (2001). doi:10.1021/bi011639y [Medline](#)
63. P. B. Rosenthal, R. Henderson, Optimal determination of particle orientation, absolute hand, and contrast loss in single-particle electron cryomicroscopy. *J. Mol. Biol.* **333**, 721–745 (2003). doi:10.1016/j.jmb.2003.07.013 [Medline](#)
64. C. Zwieb, R. W. van Nues, M. A. Rosenblad, J. D. Brown, T. Samuelsson, A nomenclature for all signal recognition particle RNAs. *RNA* **11**, 7–13 (2005). doi:10.1261/rna.7203605 [Medline](#)